Drop Dynamics on Liquid Infused Surfaces: The Role of the Lubricant Ridge

Muhammad S. Sadullah,[1] Ciro Semprebon,[2] and Halim Kusumaatmaja[1,*]

[1] *Department of Physics, Durham University, Durham, DH1 3LE, UK*
[2] *Department of Mathematics, Physics and Electrical Engineering, Northumbria University, Newcastle upon Tyne NE1 8ST, UK*

(Dated: May 21, 2018)

We employ a free energy lattice Boltzmann method to study the dynamics of a ternary fluid system consisting of a liquid drop driven by a body force across a regularly textured substrate, infused by a lubricating liquid. We focus on the case of partial wetting lubricants and observe a rich interplay between contact line pinning and viscous dissipation at the lubricant ridge, which become dominant at large and small apparent angles respectively. Our numerical investigations further demonstrate that the relative importance of viscous dissipation at the lubricant ridge depends on the drop to lubricant viscosity ratio, as well as on the shape of the wetting ridge.

INTRODUCTION

Liquid Infused Surfaces (LIS) are liquid repellent surfaces constructed by infusing a lubricant into textured substrates [1], as illustrated in Fig. 1. Drops placed on LIS move very easily under small perturbations and will shed away at a small tilting angle, regardless of their surface tensions [2]. These surfaces can also be designed to withstand high pressure and self-heal from physical damages [2], which distinguish them from other liquid repellent surfaces such as superhydrophobic surfaces [3].

LIS are relatively easy to fabricate. The primary requirements are a rough solid substrate with strong affinity toward the lubricant, and the drop needs to be immiscible to the lubricant [4]. These advantageous features have given rise to many potential industrial applications, such as to reduce energy consumption in fluid transports [5], to simplify cleaning and maintenance processes [6], to prevent damage due to fouling [7], and to annihilate product leftover for smart liquid packaging [8]. For many of these applications, efficient and effective control of the drop dynamics on LIS is required, yet to date such control remains poorly understood.

Compared to the more commonly studied cases of smooth and superhydrophobic surfaces [9–14], the main distinguishing feature of LIS is the presence of the infusing lubricant, forming a ridge as shown in Fig. 1. Thus the central aim of this work is to shed light on the role of the lubricant ridge in the dynamics of drops on LIS.

Based on thermodynamic arguments, Smith *et al.* showed that a liquid drop placed on LIS may invade the corrugation and replace the infusing lubricant, or it can sit on top of the corrugation with the lubricant present underneath the drop [15]. If the lubricant is perfectly wetting the substrate, the drop and the corrugated surface is separated by a thin film, and no pinning of the contact lines take place. However, closer inspection employing confocal microscopy revealed that this case is unlikely for a number of common lubricants, as they form in contact to the solid with a small but finite contact angle [15, 16]. As such, on one hand, the surface roughness helps to contain the lubricant; on the other hand, it is also the source of contact line pinning and contact angle hyeteresis.

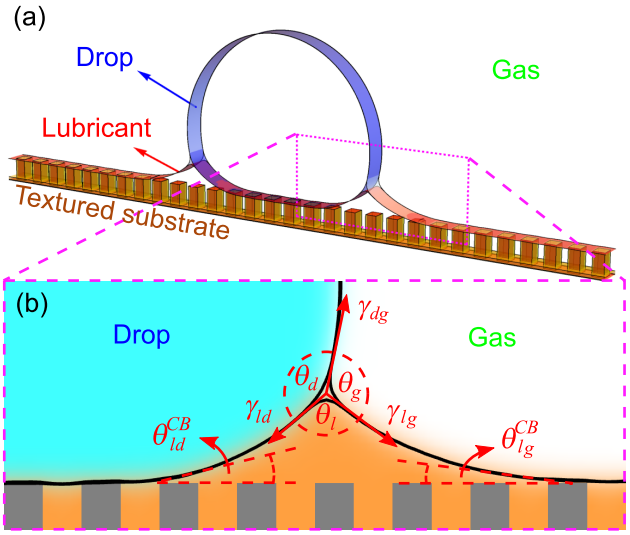

FIG. 1. (a) Rendering of a quasi 3D setup of an LIS system where a drop is sitting on a textured substrate infused with a lubricant. (b) Magnification of the lubricant ridge. γ_{dg}, γ_{lg}, and γ_{ld} are the drop-gas, lubricant-gas, and drop-lubricant surface tensions; θ_d, θ_g, and θ_l are the Neumann angles of the drop, gas and lubricant; θ_{ld}^{CB} and θ_{lg}^{CB} are the drop-lubricant and lubricant-gas contact angles assuming a Cassie-Baxter approximation.

The presence of lubricant meniscus also introduces competing dissipation mechanisms acting on a drop as it moves across LIS. For example, Keiser *et al.* have highlighted that viscous dissipation may occur predominantly in the drop or in the lubricant depending on the ratio between the drop and lubricant viscosities [17]. However, most studies to date consider only drops with apparent contact angles close to 90° [15, 17], and the impact of the shape of the lubricant meniscus on drop mobility remain unexplored. To cover such gaps, here we will investigate

these variations systematically using the lattice Boltzmann simulation method. In particular, we focus on the interplay between the contact line pinning induced by the surface corrugation and the viscous dissipation in the lubricant and drop phases.

NUMERICAL METHOD

Ternary free-energy lattice-Boltzmann method

To simulate liquid drops on LIS, we employ a ternary fluid model able to account for three bulk fluids (drop, gas and lubricant), their fluid-fluid interfacial tensions, and the fluid interactions with a solid substrate. The free energy is given by [18–20]

$$F = \sum_{m=1}^{3} \int_{\Omega} \left[\frac{\kappa_m}{2} C_m^2 (1 - C_m)^2 + \frac{\alpha^2 \kappa_m'}{2} (\nabla C_m)^2 \right] \mathrm{d}V - \sum_{m=1}^{3} \int_{\partial\Omega} h_m C_m \, \mathrm{d}S. \quad (1)$$

By construction the first term in Eq. 1 corresponds to a double well potential. Taken separately, each double well potential has minima at concentrations $C_m = 0$ (fluid component m is absent) and $C_m = 1$ (fluid component m is present). In our simulations, we initialise the system such that $\sum_{m=1}^{3} C_m = 1$ at any point in the simulation box, with three physically meaningful bulk states corresponding to the drop ($\mathbf{C} = [1, 0, 0]$), the gas ($\mathbf{C} = [0, 1, 0]$) and the lubricant ($\mathbf{C} = [0, 0, 1]$) phases.

The second term in Eq. 1 is related to the energy penalty at an interface between two fluid phases. The interfacial tension between fluid phases m and n, γ_{mn} ($m, n = 1, 2, 3$ and $m \neq n$), can be tuned by the κ_m parameters via [19]

$$\gamma_{mn} = \frac{\alpha}{6}(\kappa_m + \kappa_n), \quad (2)$$

where $\alpha = \sqrt{(\kappa_m' + \kappa_n')/(\kappa_m + \kappa_n)}$ is a parameter we can tune to vary the interface width. Typically we choose $\alpha = 1$ in our simulations.

The h_m parameters in the last term of Eq. 1 allow us to quantify the fluid-solid surface energies and correspondingly the contact angle of fluid m on a solid surface in the presence of fluid n, θ_{mn}. The contact angle θ_{mn} is given by [19]

$$\cos\theta_{mn} = \frac{\gamma_{sn} - \gamma_{sm}}{\gamma_{mn}}, \quad (3)$$

where each solid-liquid tension γ_{sm} include contribution from both majority and minority phases, expressed by the integrals I and J respectively

$$\gamma_{sm} = I_m + \sum_{n \neq m} J_n,$$
$$I_m = \frac{\alpha k_m}{12} - \frac{h_m}{2} - \frac{4h_m + k_m\alpha}{12}\sqrt{1 + \frac{4h_m}{\alpha k_m}},$$
$$J_n = \frac{\alpha k_n}{12} - \frac{h_n}{2} + \frac{4h_n - k_n\alpha}{12}\sqrt{1 - \frac{4h_n}{\alpha k_n}}.$$

For ternary fluid systems in contact with an ideal flat substrate only two out of the three contact angles are independent. For example, if θ_{12} and θ_{32} are specified, the remaining contact angle, θ_{31}, is determined by the Girifalco-Good relation [21]

$$\cos\theta_{31} = \frac{\gamma_{32}\cos\theta_{32} - \gamma_{12}\cos\theta_{12}}{\gamma_{31}}. \quad (4)$$

Any choice of the h_m parameters fulfills Eq. 4.

In our approach, we apply variable transformations from C_1, C_2 and C_3 to three equivalent order parameters, $\rho = C_1 + C_2 + C_3$, $\phi = C_1 - C_2$, and $\psi = C_3$. For simplicity, here we have set the density $\rho = 1$ everywhere. This "equal density" approximation is suitable for small Reynolds number (Re), which is the case in this work. At large Re, inertia becomes important, and the density ratios between the fluid components must be taken into account [22]. In terms of these order parameters, the equations of motion of the system are described by the continuity, Navier-Stokes and two Cahn-Hilliard equations

$$\partial_t \rho + \vec{\nabla} \cdot (\rho \vec{v}) = 0, \quad (5)$$
$$\partial_t (\rho \vec{v}) + \vec{\nabla} \cdot (\rho \vec{v} \otimes \vec{v}) = -\vec{\nabla} \cdot \mathbf{P} + \tilde{\nabla} \cdot \left[\eta (\tilde{\nabla}\mathbf{v} + \nabla\tilde{\mathbf{v}}^{\mathbf{T}}) \right], \quad (6)$$
$$\partial_t \phi + \vec{\nabla} \cdot (\phi \vec{v}) = M_\phi \nabla^2 \mu_\phi, \quad (7)$$
$$\partial_t \psi + \vec{\nabla} \cdot (\psi \vec{v}) = M_\psi \nabla^2 \mu_\psi, \quad (8)$$

where $\vec{v}$ is the fluid velocity, and η is the fluid viscosity that generally depends on the local order parameters ϕ and ψ. The latter allows us to set different viscosities for the drop, lubricant, and gas components. The thermodynamic properties of the system, described in the free energy model in Eq. 1, enter the equations of motion via the chemical potentials, $\mu_q = \delta F / \delta q$, ($q = \phi$ and ψ), and the pressure tensor, $\mathbf{P}$, defined by $\partial_\beta P_{\alpha\beta} = \phi \partial_\alpha \mu_\phi + \psi \partial_\alpha \mu_\psi$. To solve the equations of motion, Eq. 5 - 8, we employ the ternary lattice Boltzmann algorithm described in Ref. 19. More general details on the lattice Boltzmann method, including how it recovers the continuum equations of motion, can be found in Ref. 23–25.

Simulation setup

The majority of simulations are performed in a quasi three-dimensional simulation box, as shown in Fig. 1.

The dimension of the simulation box is $400 \times 10 \times 150$ LB units with the top surface bounded by a flat wall. The bottom solid surface is textured with a row of square posts of height $h = 10$ LB units, width $w = 5$ LB units, and periodicity $p = 10$ LB units. A periodic boundary condition is applied in the other two directions.

This quasi three-dimensional setup has the advantage of reducing the computational cost when compared to a full 3D simulation, while capturing the key 3D features. In the case of LIS, it preserves the essential feature of allowing the lubricant to flow in between the surface texture underneath the liquid drop. This setup has been successfully employed to study drop dynamics on flat and superhydrophobic surfaces [12, 23, 26].

The lubricant phase is initialised to fill the space between the posts and an additional layer of two lattice nodes on top of them, in order to allow the formation of a lubricant ridge at the two sides of the drop. To make sure the lubricant imbibes the bottom surface, the lubricant-drop contact angle θ_{ld} and the lubricant-gas contact angle θ_{lg} have to be smaller than the critical angle θ_c for hemi-wicking. From thermodynamic considerations it can be shown that $\cos\theta_c = (1-\phi_s)/(r-\phi_s)$, where ϕ_s and r are respectively the solid fraction and roughness factor of the surface pattern [27, 28]. The texture employed in this work gives $\phi_s = 0.25$ and $r = 3$, which leads to $\theta_c \approx 74°$.

A hemispherical drop with radius $R = 60$ LB units is placed on top of the posts and is then allowed to reach equilibrium before a body force is introduced to mobilise the drops. Unless stated otherwise, we set the horizontal and the vertical components of body force to be equal, such that $G_z = -G_x$. This choice corresponds to an experimental setup where the substrate is tilted at an angle of 45°. Adding a downward body force ensures the drop to remain attached to the substrate, especially when it has a large apparent angle. We find the steady state velocity of the drops to be insensitive to the value of G_z as long as the drop size is smaller than the capillary length, $R < l_c = \sqrt{\gamma_{dg}/\rho|G_z|}$. To characterise the drop mobility, we will take advantage of two dimensionless parameters, the Bond number $Bo = R^2 G_x/\gamma_{dg}$ and the capillary number $Ca = \eta_d V_x/\gamma_{dg}$, where γ_{dg}, η_d, and V_x are the drop-gas surface tension, drop viscosity and drop velocity parallel to the solid surface.

DROP MORPHOLOGIES IN MECHANICAL EQUILIBRIUM

In this section we will demonstrate that our ternary lattice Boltzmann approach can accurately simulate drop morphologies in mechanical equilibrium on LIS. For a liquid drop placed on an ideal smooth surface, the material contact angle, θ^Y_{dg}, is given by the Young's law, which arises from the force balance between the interfacial tensions at the three-phase contact line:

$$\cos\theta^Y_{dg} = \frac{\gamma_{sg} - \gamma_{sd}}{\gamma_{dg}}, \tag{9}$$

where γ_{sg}, γ_{sd}, and γ_{dg} are the solid-gas, solid-drop and drop-gas interfacial tensions respectively. Here we employ the superscript Y to distinguish the material contact angle from the effective contact angle under the Cassie-Baxter approximation (superscript CB).

For a drop placed on LIS, the solid-gas-drop contact line does not exist, and thus Eq. 9 does not represent a physically meaningful condition. In contrast there exist three alternative three-phase lines (see Fig. 1(b)): drop-lubricant-gas, drop-lubricant-solid, gas-lubricant-solid. To characterise how much the drop spreads on LIS, it is useful to introduce the notion of an apparent contact angle. As illustrated in Fig. 2 (top left), the apparent angle can be defined with respect to the horizontal plane at the drop-lubricant-gas triple line. In the limit of small but finite lubricant ridge, we have recently shown that the apparent angle need to satisfy the following relation [29]:

$$\frac{\sin\theta_g[\cos\theta^{CB}_{ld} - \cos(\theta_d - \theta_{app})]}{\sin\theta_d[\cos\theta^{CB}_{lg} - \cos(\theta_{app} + \theta_g)]} = \left(1 - \frac{\Delta P_{dg}}{\Delta P_{lg}}\right). \tag{10}$$

Here $\theta^{CB}_{\alpha\beta}$ is the averaged wettability expressed by the Cassie-Baxter contact angle [27],

$$\cos\theta^{CB}_{\alpha\beta} = \phi_s \cos\theta^Y_{\alpha\beta} + (1 - \phi_s), \tag{11}$$

which accounts for the fact that the drop and gas phases lie on top of a composite solid-lubricant interface. The quantity $\Delta P_{dg}/\Delta P_{lg}$ is the ratio between the Laplace pressures at the drop-gas and lubricant-gas interfaces. Since the Laplace pressure is given by $\Delta P_{\alpha\beta} = 2\gamma_{\alpha\beta}/R_{\alpha\beta}$, where $R_{\alpha\beta}$ is the mean radius of curvature for the $\alpha\beta$ interface, $\Delta P_{dg}/\Delta P_{lg}$ is directly related to the size ratio between the lubricant ridge and the drop. In the strict limit of vanishing lubricant ridge, $\Delta P_{dg}/\Delta P_{lg} \to 0$, Eq. 10 can be simplified to

$$\cos\theta_{app} = \frac{\gamma_{lg}}{\gamma_{dg}}\cos\theta^{CB}_{lg} - \frac{\gamma_{ld}}{\gamma_{dg}}\cos\theta^{CB}_{ld}. \tag{12}$$

The main advantage of Eq. 12 is that all variables on the right hand side are material parameters which can be measured independently. In contrast, the value of $\Delta P_{dg}/\Delta P_{lg}$ in Eq. 10 is usually not known a priori. However, it can be inferred from analysing the shape of the lubricant ridge.

In Fig. 2, we compare the apparent angle, θ_{app}, measured from our LB simulations once mechanical equilibrium is reached, against both the full solution in Eq. 10 and the vanishing lubricant ridge approximation in Eq. 12. The range of apparent angles are obtained by varying the surface tensions γ_{lg}, γ_{dg} and γ_{ld}, as well as

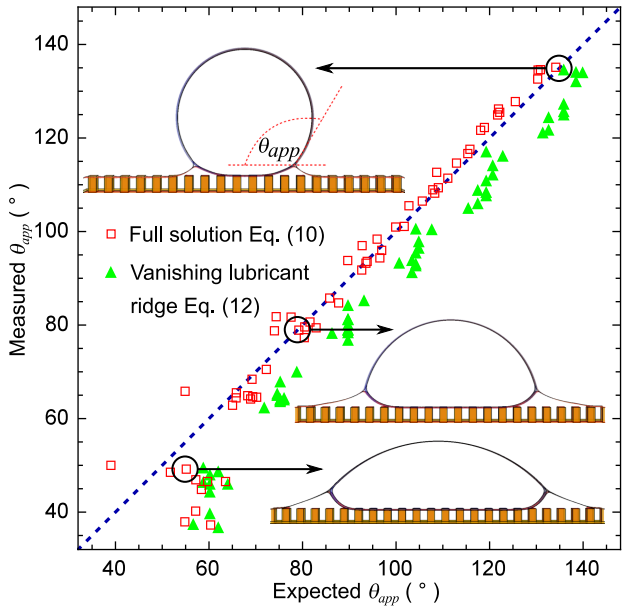

FIG. 2. Comparison between θ_{app} obtained from our simulations against the predicted values from both the full solution (Eq. 10) and the vanishing lubricant ridge approximation (Eq. 12). The top left inset illustrates how θ_{app} is measured at the drop-lubricant-gas triple line.

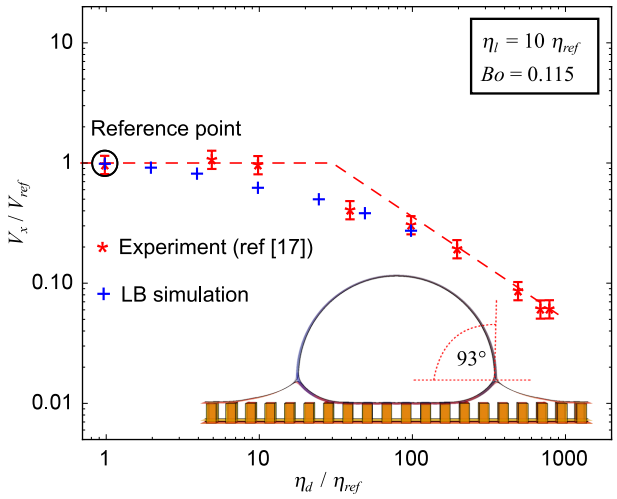

FIG. 3. Comparison between our simulation results against experimental data by Keiser *et al.* [17]. Here the lubricant viscosity is fixed at $\eta_l = 10\,\eta_{ref}$, while the drop viscosity is varied. The reference viscosity η_{ref} in the experiment is water viscosity (1 mPa.s). To ensure correct viscosity ratio between the drop and the air phases, we set $\eta_{ref} = 50\,\eta_g$ in our simulations. V_{ref} is drop velocity when $\eta_d = \eta_{ref}$.

the lubricant's material contact angles θ^Y_{lg} and θ^Y_{ld}. For comparison against the full solution (Eq. 10), we compute $\Delta P_{dg}/\Delta P_{lg}$ by measuring the radii of curvature of the drop-gas and lubricant-gas interfaces once mechanical equilibrium is reached in our simulations.

The measured apparent contact angles in our LB simulations are in very good agreement with the full solution. When compared against the vanishing lubricant ridge approximation (Eq. 12), the measured values of the apparent angle has a systematic deviation by several degrees. This deviation is expected since the size of the lubricant ridge in our simulations is not negligible compared to the drop size. Nonetheless, Eq. 12 remains a good first estimate for predicting the apparent angle of drops on liquid infused surfaces, and the accuracy improves the smaller the lubricant meniscus is compared to the drop size.

TRANSLATIONAL DROP MOBILITY

Variation in the ratio between drop and lubricant viscosities

Recent experiment by Keiser *et al.* suggests that there is a crossover between bulk drop and lubricant ridge dominated dissipation regimes, as the drop to lubricant viscosity ratio is varied [17]. Here we aim to reproduce this crossover behaviour to demonstrate that our LB simulation can correctly capture the dynamics of drops moving across LIS.

We introduce a surface patterning, surface tensions, and a body force such that $\phi_s = 0.25$, $\theta_{app} = 93°$, and $Bo = 0.115$ to mimic the experimental setup in [17] ($\phi_s = 0.23$, $\theta_{app} = 90°$, and $Bo = 0.115$). The time averaged velocities of the drop's centre of mass from our simulations are reported by the blue plus symbols in Fig. 3. The viscosity of water (about 50 times larger than the viscosity of air), $\eta_{ref} = 50\eta_g = 1$ mPa.s, is taken as the reference viscosity. We have also scaled the drop velocity by V_{ref}, taken to be the drop velocity V_x when the drop viscosity is $\eta_d = \eta_{ref}$. For comparison, the experimental data from Keiser *et al.* [17] are shown as red asterisks in Fig. 3.

For large drop viscosity, viscous dissipation lies predominantly inside the drop. In this regime, as the drop viscosity is lowered, the drop velocity increases as $V \propto \eta_d^{-1}$ [17], until it eventually plateaus to $V_x \simeq V_{ref}$. Both in simulations and experiments, the crossover occurs approximately at $\eta_d \sim 2\eta_l$. Below this value of drop viscosity, viscous dissipation in the lubricant ridge becomes dominant compared to dissipation in the drop. In this regime, the drop velocity has a strong dependence on the lubricant viscosity, while the drop viscosity has virtually no effect.

There are a number of differences between the experiments in Ref. 17 and our numerical setup. Firstly, our simulations are in quasi 3-D, rather than full 3-D. Secondly, the size of the lubricant ridge compared to the drop size is larger than that in experiments. Thirdly, we have considered partial wetting lubricant, $\theta_{wet} = 45°$, whereas the experiments were done using a complete wetting lu-

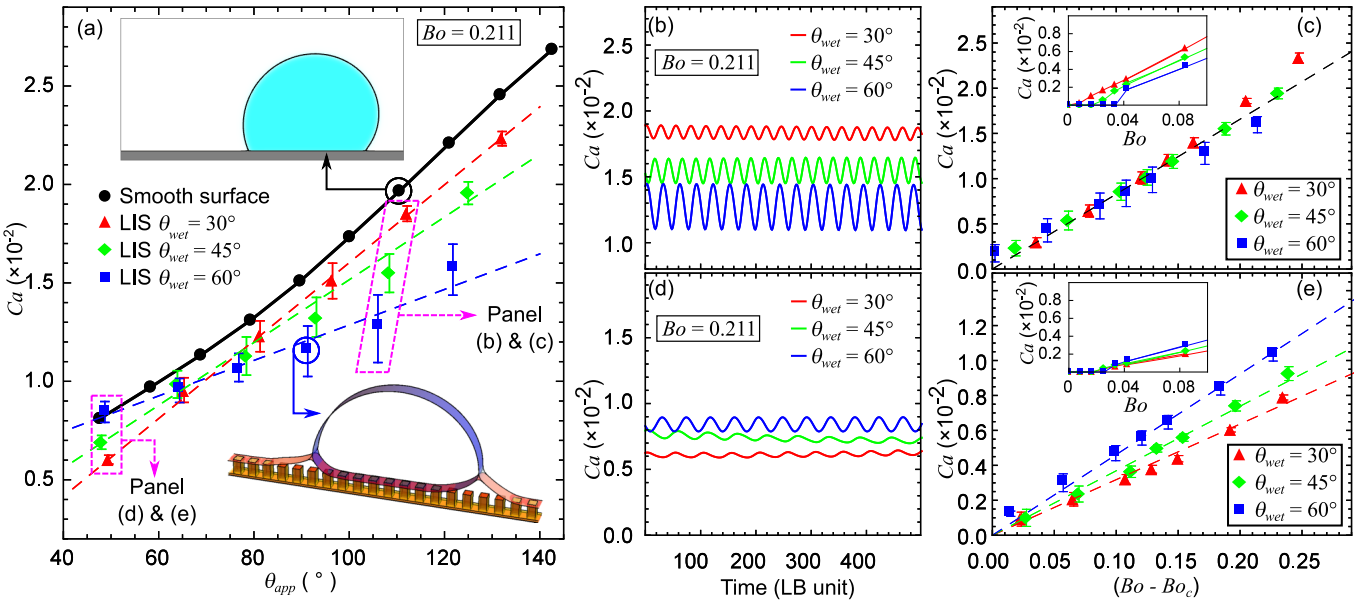

FIG. 4. (a) Drop mobility on smooth surface (black dots) and LIS (red triangles, green diamonds, and blue squares) plotted against θ_{app}. θ_{wet} is the wetting angle of the lubricant phase ($\theta_{lg}^{Y} = \theta_{ld}^{Y} = \theta_{wet}$). The drop mobility is represented by the capillary number Ca. (b) and (d) drop mobility versus time for the cases indicated in panel (a). The capillary number Ca increases and decreases periodically due to pinning-depinning events. (c) and (e) drop mobility for cases indicated in panel (a) as a function of $Bo - Bo_c$. Bo is the Bond number. The insets show the critical Bond number, Bo_c, at which the drops start moving under external body force.

bricant, $\theta_{wet} = 0°$. Nonetheless, it is clear from Fig. 3 that the crossover between bulk drop and lubricant ridge dominated dissipation regimes is a robust phenomenon, which our simulations can accurately capture.

Variation in apparent and wetting angles

In the previous section we numerically verified the crossover between viscous friction in the bulk drop and in the lubricant ridge. The similarity between experiments and numerical simulations is valid despite the fact we employed partial wetting lubricants, which involve also pinning and depinning effects. In this section we will focus on the role of lubricant wettability on the drop mobility, in particular on the interplay between contact line pinning and viscous friction.

As a reference case, we first consider a drop moving on a flat surface as illustrated in the top-left inset of Fig. 4(a). The viscosity of the drop is set to be $\eta_d = 50\eta_g$ to mimic a water drop in a dry air environment. A constant body force with $Bo = 0.211$ is then applied to mobilise the drop so that the drop moves and reaches a steady state velocity. The results obtained for drops on a smooth surface are represented by black dots in Fig. 4(a) as a function of the contact angle. For a smooth surface, we identify $\theta_{app} = \theta_{dg}^{Y}$. In agreement with previous studies, the steady state capillary number of the drop increases monotonically with θ_{app} [13, 14], due to the decrease in wedge dissipation at the contact line.

Let us now consider the equivalent setup for drops on LIS, as illustrated in the bottom-right inset of Fig. 4(a). The lubricant viscosity η_l is set to be the same as the drop viscosity, $\eta_l = \eta_d = 50\eta_g$. To reduce the number of parameters to be explored in our simulations, we will assume a symmetric wetting condition for the lubricant, where $\theta_{lg}^{Y} = \theta_{ld}^{Y} = \theta_{wet}$.

For a given θ_{wet} we systematically vary the drop apparent angle, θ_{app}, by tuning the fluid-fluid surface tensions, and consequently the Neumann angles, θ_l, θ_d and θ_g. In Fig. 4(a) we compare the drop mobility, quantified as the time-averaged capillary number Ca for $\theta_{wet} = 30°$ (red triangles), $\theta_{wet} = 45°$ (green diamonds), and $\theta_{wet} = 60°$ (blue squares). Similar to the smooth surface case, the drop mobility increases monotonically with the apparent angle, but the magnitude of the Ca is generally smaller than for a smooth surface. Interestingly, when comparing the three datasets for different θ_{wet}, we observe that, while for larger θ_{app} drops with smaller θ_{wet} move faster than those with larger θ_{wet}, this ordering is reversed for lower θ_{app}. The presence of these two regimes (for lower θ_{app} and larger θ_{app}) is persistent for different values of Bo, η_d and η_l.

We hypothesise this ordering inversion is due to a shift in the relative importance between viscous dissipation and contact line pinning at the lubricant ridge. To better characterise the pinning-depinning effects during drop motion, we plot the instantaneous Ca associated to the

drop's centre of mass, as a function of time for three drops with $\theta_{app} \sim 110°$ and $\theta_{app} \sim 45°$ respectively in Figs. 4(b) and 4(d). We observe that the instantaneous Ca oscillates periodically, which is due to pinning-depinning events as the drop moves across the periodic LIS pattern (see ESI video). For both large (Fig. 4(b)) and small (Fig. 4(d)) θ_{app}, the oscillations with larger amplitude are always observed for higher θ_{wet}. At the same time, the amplitude of the oscillations is generally smaller for $\theta_{app} \sim 45°$ than for $\theta_{app} \sim 110°$, which implies a less pronounced effect of pinning and depinning.

To further assess the relative importance of pinning versus viscous dissipation, we explore the relation between the driving force and the drop velocity for both cases of $\theta_{app} \sim 110°$ (Fig. 4(c)) and $\theta_{app} \sim 45°$ (Fig. 4(e)). Assuming a linear approximation, the relation between Ca, Bo and Bo_c can be expressed as $Ca = (Bo - Bo_c)/\beta$ [15, 30, 31]. Bo_c, the largest Bond number at which the drop remains stationary, is a measure of contact line pinning, or alternatively, contact angle hysteresis. β is a function of the shapes of the drop and lubricant meniscus, and it is related to their rate of viscous dissipation.

Considering Ca as a function of $(Bo - Bo_c)$, our data show an important difference between the large and small apparent angle drops. For large apparent angles (Fig. 4(c)), all the curves practically overlap onto a master curve. The variations in the results for $\theta_{wet} = 30°$ (red triangles), 45° (green diamonds), and 60° (blue squares) can be captured by differences in the value of the critical Bond number, Bo_c, as shown in the inset. This indicates that the ordering observed in Fig. 4(a) for large θ_{app} is determined by contact line pinning. The prefactor β is the same for the three datasets in Fig. 4(c), which suggest that the rate of viscous dissipation is on average the same once the reduction in the effective driving force due to pinning forces is taken into account.

In contrast, for small apparent angles (Fig. 4(e)), the datasets do not overlap onto a master curve. The critical Bond number, Bo_c, is also essentially the same – any differences observed are within the error of the measurements – for the three θ_{wet} used. These two observations suggest that, for low θ_{app}, contact line pinning plays a minor role. The variations in Ca vs $(Bo - Bo_c)$ for the three datasets in θ_{wet} further imply that viscous dissipation is larger for the more wetting lubricant. Inspection of the drop morphologies supports this observation. We find that, for large θ_{app}, the lubricant ridges have similar shape, regardless of θ_{wet}. In contrast for low θ_{app} the ridge shape is broader for lower θ_{wet} (ESI document, SFig. 1 and SFig. 2).

To further corroborate this hypothesis, we ran three additional sets of simulations, where pinning and depinning is inhibited by replacing the topography with a flat substrate, as shown in Fig. 5. The three sets correspond to $\theta_{wet} = 30°$ (red triangles), $\theta_{wet} = 45°$ (green diamonds), and $\theta_{wet} = 60°$ (blue squares). The amount of lubricant in both the front and back ridge is the same for all cases. Accordingly, once pinning is removed, drops with higher θ_{wet} always move faster irrespective of θ_{app}, showing the same ordering that we obtain only for low θ_{app} in Fig. 4(a).

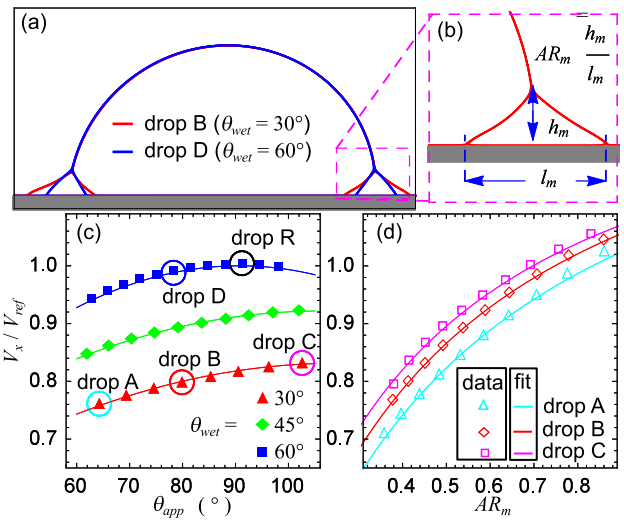

FIG. 5. (a) In the absence of contact line pinning, drops with higher θ_{wet} always move faster. (b) Comparison of drop shapes with the same θ_{app} but different θ_{wet} and correspondingly meniscus aspect ratio AR_m. (c) Definition of AR_m. (d) Drop mobility against AR_m for different θ_{app}. The lines are the best fit results to Eq. 15. V_{ref} is taken to be the velocity of drop R in panel (a).

Fig. 5(a) compares the morphologies of drops B and D indicated in Fig. 5(c). The two drops have an almost identical shape and θ_{app}, but their lubricant ridge shapes and mobilities are different. For drop B, θ_{wet} is smaller, and therefore the meniscus is broader. We can characterise the meniscus shape by its aspect ratio, defined as $AR_m = h_m/l_m$, where h_m and l_m are its height and length respectively, see Fig. 5(b).

We now propose a scaling argument to explain how the drop mobility depends on the lubricant ridge aspect ratio. We balance the rate of energy injected by the applied body force with the total rate of energy dissipation in the drop and lubricant,

$$FV_x \sim \eta_d \int |\nabla v|_d^2 dA_d + \eta_l \int |\nabla v|_l^2 dA_l. \qquad (13)$$

Here F is the total force acting on the drop. We also recall that the simulations in Fig. 5 are two-dimensional simulations; thus the terms on the right hand side are integrated over the drop and the lubricant ridge area. Taking $|\nabla v|_d \sim V_x/R$ and $|\nabla v|_l \sim V_x/h_m$ as the typical velocity gradient in the drop and lubricant meniscus, as well as $\Delta A_d \sim R^2$ and $\Delta A_l \sim h_m l_m$ as the typical scales for the cross-sectional area of the drop and the lubricant,

we have

$$F \sim \alpha_d \eta_d V_x + \alpha_l \eta_l V_x l_m / h_m, \quad (14)$$

$$V_x \sim \frac{F}{\alpha_d \eta_d + \alpha_l \eta_l / AR_m}. \quad (15)$$

where α_d and α_l are positive, dimensionless fitting parameters. Eq. 15 shows that a smaller AR_m results in a larger energy dissipation in the lubricant meniscus, which in turn leads to the lower mobility of the drop.

In Fig. 5(d), we consider drops A, B and C indicated in Fig. 5(c), and increase their AR_m by tuning θ_{wet}. We keep all other variables in the simulations the same, including the body force, the fluid surface tensions, the lubricant and drop viscosities, and the total drop and lubricant cross-sectional area. The data points in Fig. 5(d) correspond to simulation results, while the lines correspond to the best fit results to Eq. 15, where we have fitted α_d and α_l separately for each dataset. Consistent with our scaling argument, for all of the three datasets in Fig. 5(d), drop mobility increases monotonically with AR_m.

Taking advantage of the results in Fig. 5, we can robustly conclude that the ordering observed in Fig. 4(a) for small θ_{app} is due to variations in viscous dissipation at the lubricant ridge. For the present choice of viscosities $\eta_l = \eta_d = 50\eta_g$, the crossover between pinning and meniscus viscous friction dominated regimes in Fig. 4(a) occurs at $\theta_{app} \simeq 70°$. In ESI SFig. 3, we take the limit where the lubricant viscosity is very low, equal to the gas viscosity. In this case viscous dissipation at the lubricant is weak compared to that in the drop. As expected, for low apparent angle θ_{app}, we then observe that the drop mobilities remain very similar as we vary the wetting angle θ_{wet}.

CONCLUSIONS

In this work we have employed a computational method, based on the free energy lattice Boltzmann approach, to study drop dynamics on LIS. We show that the drop apparent angle on LIS can be captured accurately. Despite differences compared to typical experiments, namely the cylindrical geometry and the relatively larger size of the lubricant ridge, the drop mobility computed from our simulations shows a remarkable agreement with the experiments by Keiser *et al.*[17], as the drop and lubricant viscosity ratio is varied. Furthermore we have considered the more complex case of partially wetting lubricants, and revealed a rich interplay between contact line pinning and viscous friction. Specifically, we have shown that for large apparent angles contact line pinning dominates, and drops with more wetting lubricants move faster. In contrast, for small apparent angles viscous friction in the lubricant ridge dominates. The magnitude of the viscous dissipation is determined by the shape of the lubricant ridge, and as such, drops in LIS with less wetting lubricants move faster.

To our best knowledge this is the first simulation study of drops on LIS that accounts for the full dynamics of the fluid flows. The lattice Boltzmann method we have employed here is versatile, and there are a number of avenues of future numerical work. In this work we have assumed a LIS substrate textured with a regular periodic pattern of pillars, while many LIS substrates are constructed experimentally using irregular topographies [2, 15, 16, 32]. The impact of random roughness on the drop dynamics will be investigated in a forthcoming study. It has also been pointed out that drainage of the infusing lubricant is a major source of failure for LIS technology [33, 34]. As such, our approach is suitable for investigating how the surface topographies can be designed to minimise the loss of lubricant during drop motion.

ACKNOWLEDGEMENT

MSS is supported by an LPDP (Lembaga Pengelola Dana Pendidikan) scholarship from the Indonesian Government. HK acknowledges funding from EPSRC (grant EP/P007139/1) and Procter & Gamble. CS acknowledges support from Northumbria University through the Vice-Chancellor's Fellowship Programme. We thank Matthew Wagner and Yonas Gizaw for useful discussions.

* halim.kusumaatmaja@durham.ac.uk

[1] D. Quéré, Rep. Prog. Phys. **68**, 2495 (2005).
[2] T.-S. Wong, S. H. Kang, S. K. Y. Tang, E. J. Smythe, B. D. Hatton, A. Grinthal, and J. Aizenberg, Nature **477**, 443 (2011).
[3] M. Ma and R. M. Hill, Curr. Opin. Colloid Interface Sci. **11**, 193 (2006).
[4] P. Kim, M. J. Kreder, J. Alvarenga, and J. Aizenberg, Nano Lett. **13**, 1793 (2013).
[5] N. J. Shirtcliffe, G. McHale, M. I. Newton, and Y. Zhang, ACS Appl. Mater. Interfaces **1**, 1316 (2009).
[6] Y. Lu, S. Sathasivam, J. Song, C. R. Crick, C. J. Carmalt, and I. P. Parkin, Science **347**, 1132 (2015).
[7] M. Ferrari, A. Benedetti, E. Santini, F. Ravera, L. Liggieri, E. Guzman, and F. Cirisano, Colloids Surf. A **480**, 369 (2015).
[8] `https://www.youtube.com/watch?v=djwahGRi5iE`.
[9] D. Richard and D. Quéré, Europhys. Lett. **48**, 286 (1999).
[10] L. Mahadevan and Y. Pomeau, Phys. Fluids **11**, 2449 (1999).
[11] S. R. Hodges, O. E. Jensen, and J. M. Rallison, J. Fluid Mech. **512**, 95 (2004).
[12] B. M. Mognetti, H. Kusumaatmaja, and J. M. Yeomans, Faraday Disc. **146**, 153 (2010).
[13] S. P. Thampi, R. Adhikari, and R. Govindarajan, Langmuir **29**, 3339 (2013).
[14] N. Moradi, F. Varnik, and I. Steinbach, Europhys. Lett. **95**, 44003 (2011).

[15] J. D. Smith, R. Dhiman, S. Anand, E. Reza-Garduno, R. E. Cohen, G. H. McKinley, and K. K. Varanasi, Soft Matter **9**, 1772 (2013).

[16] F. Schellenberger, J. Xie, N. Encinas, A. Hardy, M. Klapper, P. Papadopoulos, H.-J. Butt, and D. Vollmer, Soft Matter **11**, 7617 (2015).

[17] A. Keiser, L. Keiser, C. Clanet, and D. Quéré, Soft Matter **13**, 6981 (2017).

[18] J. Kim, Computer Methods in Applied Mechanics and Engineering **196**, 4779 (2007).

[19] C. Semprebon, T. Krüger, and H. Kusumaatmaja, Phys. Rev. E **93**, 033305 (2016).

[20] S. Dong, Journal of Computational Physics **361**, 1 (2018).

[21] L. Girifalco and R. Good, J. Phys. Chem. **61**, 904 (1957).

[22] M. Wöhrwag, C. Semprebon, A. M. M., I. Karlin, and H. Kusumaatmaja, arXiv:1710.07486.

[23] H. Kusumaatmaja and J. M. Yeomans, in *Simulating Complex Systems by Cellular Automata*, edited by A. G. Hoekstra, J. Kroc, and P. M. A. Sloot (Springer-Verlag, Heidelberg, 2010) Chap. 11, pp. 241–274.

[24] S. Succi, *The Lattice Boltzmann Equation* (Oxford University Press, Oxford, 2001).

[25] T. Kruger, H. Kusumaatmaja, A. Kuzmin, O. Shardt, G. Silva, and E. Viggen, *The Lattice Boltzmann Method: Principles and Practice* (Springer International Publishing, Switzerland, 2017).

[26] N. Moradi, F. Varnik, and I. Steinbach, Europhys. Lett. **89**, 26006 (2010).

[27] D. Quéré, Annu. Rev. Mater. Res. **38**, 71 (2008).

[28] C. Semprebon, P. Forsberg, C. Priest, and M. Brinkmann, Soft Matter **10**, 5739 (2014).

[29] C. Semprebon, G. McHale, and H. Kusumaatmaja, Soft Matter **13**, 101 (2017).

[30] S. Varagnolo, D. Ferraro, P. Fantinel, M. Pierno, G. Mistura, G. Amati, L. Biferale, and M. Sbragaglia, Phys. Rev. Lett. **111**, 066101 (2013).

[31] C. Semprebon and M. Brinkmann, Soft Matter **10**, 3325 (2014).

[32] J. T. Luo, N. R. Geraldi, J. H. Guan, G. McHale, G. G. Wells, and Y. Q. Fu, Phys. Rev. Applied **7**, 014017 (2017).

[33] J. S. Wexler, I. Jacobi, and H. A. Stone, Phys. Rev. Lett. **114**, 168301 (2015).

[34] J.-H. Kim and J. P. Rothstein, Exp. Fluids **57**, 81 (2016).